Orbital evolution of satellite galaxies in self-interacting dark matter models

Oren Slone[®], ^{1,2,*,†} Fangzhou Jiang[®], ^{3,4} Mariangela Lisanti[®], ¹ and Manoj Kaplinghat[®] ¹Department of Physics, Princeton University, Princeton, New Jersey 08544, USA ²Department of Physics, Center for Cosmology and Particle Physics, New York University, New York, New York 10003, USA ³TAPIR, California Institute of Technology, Pasadena, California 91125, USA ⁴Carnegie Observatories, 813 Santa Barbara Street, Pasadena, California 91101, USA ⁵University of Irvine, Irvine, California 92697, USA

(Received 17 September 2021; revised 6 December 2022; accepted 10 January 2023; published 10 February 2023)

Dark matter self-interactions can leave distinctive signatures on the properties of satellite galaxies around Milky Way-like hosts through their impact on tidal stripping, ram pressure, and gravothermal collapse. We delineate the regions of self-interacting dark matter parameter space—specified by interaction cross section and a velocity scale—where each of these effects dominates and show how the relative mass loss depends on the satellite's initial mass, density profile, and orbit. We obtain novel, conservative constraints in this parameter space using Milky Way satellite galaxies with notably high central densities and small pericenter distances. Our results for self-interacting dark matter models, in combination with constraints from clusters of galaxies, favor either velocity-dependent cross sections that lead to gravothermal core collapse in the densest satellites or small cross sections which more closely resemble cold and collisionless dark matter.

DOI: 10.1103/PhysRevD.107.043014

I. INTRODUCTION

Current observational efforts are characterizing properties of satellite galaxies orbiting the Milky Way (MW) [1,2] and other hosts [3,4]. This wealth of new data provides an exciting opportunity to test the evolution of small-scale structure in self-interacting dark matter (SIDM) [5–18], as compared to cold dark matter (CDM) [19–24]. SIDM arises generically in many theories [25] and is well motivated from an astrophysical standpoint [26–29]. In this study, we present a first analysis of the impact of velocity-dependent, anisotropic scattering between dark matter (DM) particles on the orbits of satellite galaxies.

For CDM, many ingredients affect satellite orbits including initial positions and velocities, as well as initial masses and concentrations, which affect mass loss due to tidal forces and orbital decay due to dynamical friction. For SIDM, these continue to play a role, while mass removal and momentum transfer from DM ram pressure also impact the evolution [30]. The density profile of an SIDM satellite is also critical to its evolution. The presence of a constant density, quasistable, isothermal core can increase the amount of mass that is tidally removed [7]. This core can also undergo gravothermal collapse with a timescale that depends on various factors.

Corresponding author. oslone@princeton.edu os2124@nyu.edu

High concentration satellites collapse faster [12,31], with tidal stripping [11] and high cross sections [10] accelerating this process. The collapse can dramatically increase the central densities of satellites [12,14,31–36], which may be necessary for SIDM to be consistent with inferred densities of ultrafaint dwarfs [10,12,37].

We perform a conceptual analysis using semianalytical orbit integration to map the consequences of SIDM on satellite orbital evolution. In particular, the parameter space for which mass loss in SIDM is dominated by either tidal stripping or ram-pressure evaporation is identified. In the former case, the signature is an overall mass reduction in the satellite's outer region, as compared to CDM. In the latter case, ram-pressure evaporation also removes mass from the satellite's central regions, causing lower central densities than would be expected for CDM. We also identify regions where the effects of gravothermal collapse are important. These findings motivate new observational handles for testing SIDM.

We begin with an overview of modeling satellite orbital evolution. We then discuss qualitative signatures of SIDM on satellite distributions around MW-like hosts. Building on this understanding, we set novel and conservative SIDM constraints using measured properties of MW dwarfs. The interested reader can find the precise details of our modeling in the Appendices and should note that effects not accounted for in our modeling do not change any qualitative results of the study and keep quantitative results conservative. We have compared the results of our modeling to results from the simulations of Ref. [21] and find qualitative agreement.

II. SATELLITE EVOLUTION

This study considers scenarios where DM particles of mass m_{χ} interact via a light scalar/vector mediator of mass m_{ϕ} with coupling α_D [38–40]. In the nonrelativistic limit, elastic self-scattering is well described by a Yukawa potential. When $\alpha_D m_{\chi}/m_{\phi} \ll 2\pi$, the cross section can be calculated using the Born approximation,

$$\frac{d\sigma}{d\theta} = \frac{\sigma_0 \sin \theta}{2 \left[1 + \frac{v^2}{\omega^2} \sin^2 \frac{\theta}{2} \right]^2},\tag{1}$$

(however see Ref. [41]) where $\sigma_0 \equiv 4\pi\alpha_D^2 m_\chi^2/m_\phi^4$, $\omega \equiv m_\phi/m_\chi$, and v is the velocity difference between interacting particles (σ_m or σ_{0m} will be used as shorthand for σ/m_χ or σ_{0}/m_χ , respectively; in all equations we use the convention c=1). Satellites are useful probes of Eq. (1) because interactions between satellite and host probe velocities of order $\mathcal{O}(100)$ km/s, while interactions within the satellite probe velocities of order $\mathcal{O}(10)$ km/s.

The three ingredients needed to properly model the evolution of in-falling satellites are as follows.

A. Host and satellite density profiles

Thermalization and heat flow resulting from self-interactions alter DM density profiles [42]. Any initially cuspy halo will exhibit inward heat flow, resulting in a semistable isothermal configuration within the region where SIDM interactions are rapid. When baryons are unimportant, as is typically the case for low-mass satellites, the density profile develops a core at a radius r_c and transitions to a Navarro-Frenk-White (NFW) profile [43] beyond. We model the enclosed mass of such a profile as

$$M_{\text{SIDM}}(r) = M_{\text{NFW}}(r) \cdot \tanh\left(\frac{r}{r_c}\right),$$
 (2)

where $M_{\rm NFW}(r)$ is the enclosed mass of an NFW profile (with normalization ρ_0 and scale radius r_s), the core radius is defined as $r_c = \min{[0.5r_1, r_s]}$, and r_1 is the radius below which interactions occur at least once within the age of the halo (see Appendix A for details). This form of the enclosed mass has an analytical solution for the density profile [found by differentiating Eq. (2)] and also has the same total enclosed mass at $r \gg r_c$ as that of an NFW profile with the same ρ_0 and r_s . For a MW-like host, the presence of baryons leads to a cuspy profile that resembles an NFW profile with scale radius r_s [44,45]. We model such profiles, as well as profiles for a CDM model, as NFW profiles. The results of this study do not include the effects of the MW's stellar disk on subhalos [20,23,24,46,47],

which requires a more sophisticated treatment. We can include the impact of an additional spherical potential (to partially mimic the stellar disk for the assumed orbits), but we find that its effects are small—see additional discussion below and in Appendix C. We expect that the bound derived in Sec. III C will be more stringent when all the relevant physics is included.

This semistable configuration with an isothermal core does not remain intact indefinitely. Eventually, heat flow changes direction, transferring heat outward. Because the core has negative specific heat, this results in a runaway gravothermal collapse process whereby the core heats up and shrinks simultaneously [32]. An important distinction should be made between the case when the SIDM mean free path is either longer (LMFP) or shorter (SMFP) than the Jeans length of the core. In the LMFP regime, heat escapes efficiently from the core and the timescale for gravothermal collapse is $t_{\rm GC} \approx 290/(\langle \sigma_m v \rangle \rho_{\rm core})$, where $\rho_{\rm core}$ is the core density [32] (tidal stripping can significantly shorten t_{GC} by enhancing the rate of heat flow [12,36]). In this phase, the density profile has a shrinking core radius r_c . Outside r_c , the density decreases approximately as $r^{-2.19}$ and transitions to the NFW profile when $r \gtrsim r_s$ [32] for isolated halos. In the SMFP regime, heat gets trapped in the core and collapse occurs much more rapidly. Importantly, gravothermal collapse in the LMFP regime cannot produce arbitrarily large densities at a given radius because the evolution of the profile is such that the core density increases while the core size shrinks. To model the scenario of a halo that initially thermalizes and cores below r_c and eventually undergoes collapse in the LMFP regime, we use a phenomenological profile of the form

$$\rho_{\rm GC}(r) = \frac{\rho_0}{(r/r_{\rm GC})^{\alpha} (1 + r/r_{\rm GC})^{3-\alpha}} \tanh\left(\frac{r}{\min[r_c, r_{\rm GC}]}\right)^{\alpha},\tag{3}$$

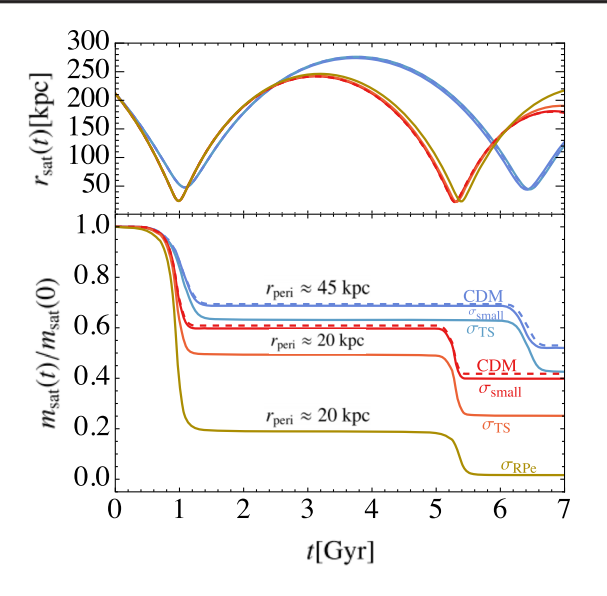
where $\alpha = 2.19$ and $r_{GC} = 2r_s$ (see Appendix A for details).

B. Mass loss

Satellite mass loss occurs predominantly via tidal stripping and ram-pressure evaporation. The former is a result of host tidal forces that strip material from the satellite, located at position r. These forces are efficient above the tidal radius ℓ_t (measured from the satellite's center),

$$\ell_t \approx r \left(\frac{1}{g(r)} \frac{m_{\text{sat}}(\ell_t)}{M_{\text{host}}(r)} \right)^{1/3},$$
 (4)

where $m_{\rm sat}(\ell)$ and $M_{\rm host}(r)$ are the satellite and host enclosed masses, respectively, and g(r) accounts for both the tidal force and centrifugal force acting on the satellite, as described in Eq. (A6) of Appendix A [48,49]. The approximate mass-loss rate resulting from tidal stripping is



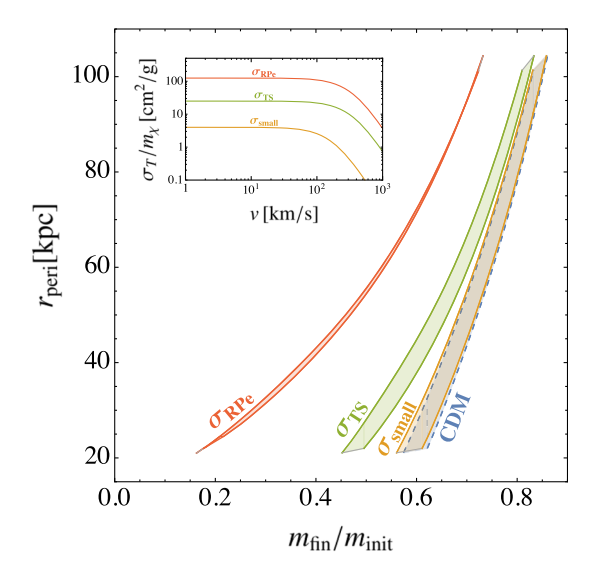


FIG. 1. Satellite evolution around a $10^{12}M_{\odot}$ host. Left: time evolution of satellite mass (bottom) and radial position (top), assuming $m_{\rm init} = 10^{10}M_{\odot}$, for CDM (dashed) and SIDM with initial isothermal cores (solid). The SIDM parameters $\{\sigma_{0m}, \omega\}$ correspond to $\sigma_{\rm small} = \{4~{\rm cm^2/g}, 160~{\rm km/s}\}$, $\sigma_{\rm TS} = \{25~{\rm cm^2/g}, 315~{\rm km/s}\}$, and $\sigma_{\rm RPE} = \{125~{\rm cm^2/g}, 315~{\rm km/s}\}$. We contrast results for an eccentric orbit with pericenter $r_{\rm peri} \approx 20~{\rm kpc}$ with that of $r_{\rm peri} \approx 45~{\rm kpc}$. Relative to CDM, SIDM results in increased mass loss, especially in the case of more radial orbits. Right: comparison of satellite mass loss in various scenarios. Initial satellite masses are considered in the range $m_{\rm init} \in [10^9, 10^{10.5}]M_{\odot}$ corresponding to the width of each band. Satellites are placed on orbits with varying pericenters and evolved for one pericentric passage. The ratio of final to initial mass is given on the horizontal axis; the four bands correspond to CDM, $\sigma_{\rm small}$, $\sigma_{\rm TS}$, and $\sigma_{\rm RPE}$. The inset shows the velocity dependence of the transfer cross section for each SIDM scenario.

$$\dot{m}_{\rm TS} \approx -A \frac{m_{\rm sat}(>\ell_t)}{t_{\rm dvn}(r)},$$
 (5)

where $\mathcal{A}=0.55$ [50], $m_{\rm sat}(>l_t)\equiv m_{\rm sat}-m_{\rm sat}(\ell_t)$, and $t_{\rm dyn}(r)$ is the dynamical time [51]. The tidal radius is strongly dependent on the satellite's density profile. Comparing a cored SIDM to an NFW profile, one finds that, when $\ell_t \lesssim r_c$, the tidal radius shrinks rapidly for SIDM, resulting in more efficient tidal stripping compared to CDM.

Ram-pressure evaporation (RPE) is the result of host-satellite DM interactions. For any scattering event, if a particle's final velocity is larger than the escape velocity of the satellite $v_{\rm esc}$, the particle evaporates. The resulting mass-loss rate is

$$\dot{m}_{\rm RPE} \approx -m_{\rm sat} \eta_e \sigma_m v_{\rm sat} \rho_{\rm host},$$
 (6)

where $v_{\rm sat}$ is the satellite's velocity relative to the host, $\rho_{\rm host}$ is the DM density of the host at position r, and η_e is the $\mathcal{O}(1)$ evaporation fraction [30]. For cases of interest, most host-satellite scattering events result in evaporation and the evaporation fraction is just unity, $\eta_e \approx 1$.

C. Orbits

Assuming that the satellite is not significantly deformed by tidal forces and treating it as a point, the orbit is obtained by evaluating the equation of motion,

$$\mathbf{a}_{\text{tot}} = -\nabla \Phi + \mathbf{a}_{\text{DF}} + \mathbf{a}_{\text{RPd}},\tag{7}$$

where Φ is the gravitational potential of the host, \mathbf{a}_{DF} is the acceleration due to dynamical friction [52] (modeled using the Chandrasekhar formula), and \mathbf{a}_{RPd} is the acceleration due to ram pressure. The latter arises from momentum transfer to the satellite from host-satellite SIDM scatterings and is given by

$$\mathbf{a}_{\text{RPd}} \approx -\mathbf{v}\eta_d \sigma_m v_{\text{sat}} \rho_{\text{host}},$$
 (8)

where η_d is the deceleration fraction [30] [see Eq. (A13) and discussion around it]. When $v_{\rm sat}$ is of order the virial velocity of the host, η_d decreases rapidly as $\eta_d \propto (v_{\rm esc}/v_{\rm sat})^2$. Thus, work done by ram-pressure deceleration is only comparable to dynamical friction for large σ_{0m} and ω (see Fig. 5). Full details are provided in Appendix A.

III. RESULTS

A. Orbit-mass relations

Figure 1 (bottom left) demonstrates the mass evolution of a $10^{10} M_{\odot}$ satellite for different DM model assumptions. The satellite is initialized at the virial radius and virial velocity of a $10^{12} M_{\odot}$ host at z=1, and two classes of orbits (with differing initial angular momenta) are considered with pericenters at $r_{\rm peri} \approx 20$ and 45 kpc (the top panel shows the satellites' radial positions $r_{\rm sat}$ as functions of

time). Dashed curves show results for CDM, while solid curves show results for three different sets of SIDM parameters, denoted as $\sigma_{\rm small}$, $\sigma_{\rm TS}$, and $\sigma_{\rm RPE}$ (defined in the caption). $\sigma_{\rm small}$ gives results that are similar to CDM. For $\sigma_{\rm TS}$, tidal stripping effects are more important for SIDM than for CDM. For $\sigma_{\rm RPE}$, the ram-pressure evaporation rate strongly exceeds that of tidal stripping. Generally, satellite mass loss is more pronounced for SIDM than CDM, especially for larger interaction cross sections and more eccentric orbits.

The example of σ_{RPE} is particularly noteworthy. After its first pericentric passage, ~80% of the satellite's mass is removed. The primary difference relative to σ_{small} and σ_{TS} is that mass loss due to ram-pressure evaporation dominates over tidal stripping, enhancing even further the difference between CDM and SIDM. While the latter preferentially removes mass from the outermost regions of the galaxy, the former has a more noticeable impact on its inner regions. This suggests that one can use observations of dwarf galaxies with low pericenters and high central densities to constrain SIDM.

We estimate the effects of the MW's stellar disk on the tidal stripping rate by reproducing Fig. 1 (left) with the inclusion of a $10^{11}M_{\odot}$ point mass at the MW's center. The result is shown in Fig. 7. For the three reference cross sections, the mass-loss difference is of order 10% or less of $m_{\rm sat}(0)$. We defer a detailed analysis of these effects to future work.

Figure 1 (right) demonstrates in more detail how mass loss over one pericentric passage varies as a function of the SIDM parameters, the initial satellite mass m_{init} , and the pericentric radius r_{peri} . Such results can potentially be used to infer microscopic properties of DM from observations such as the distribution of satellites around their hosts. The four bands correspond to CDM (dashed) and the three SIDM cross sections of the left panel (solid). From right to left across each band, the initial masses span $m_{\rm init} \in [10^9, 10^{10.5}] M_{\odot}$. The results show that tidal stripping is more effective at creating differences between SIDM and CDM for larger mass satellites with smaller pericenters. The reason for this is twofold. First, the more massive a satellite, the more dynamical friction it experiences, causing its pericenter to decrease. Second, more massive satellites have larger values of r_c , which further enhance tidal stripping. For σ_{RPE} , a sizable difference is already observed for large pericenters and for small pericenters the difference is dramatic, with SIDM satellites losing large fractions of their mass.

B. SIDM parameter space

In Fig. 2, we build a conceptual map in SIDM parameter space showing where various mechanisms dominate a satellite's evolution. Colored areas demarcate regions of interest for satellites with $m_{\rm init} \in [10^9, 10^{10}] M_{\odot}$ orbiting about a $10^{12} M_{\odot}$ host. The concentration of each satellite

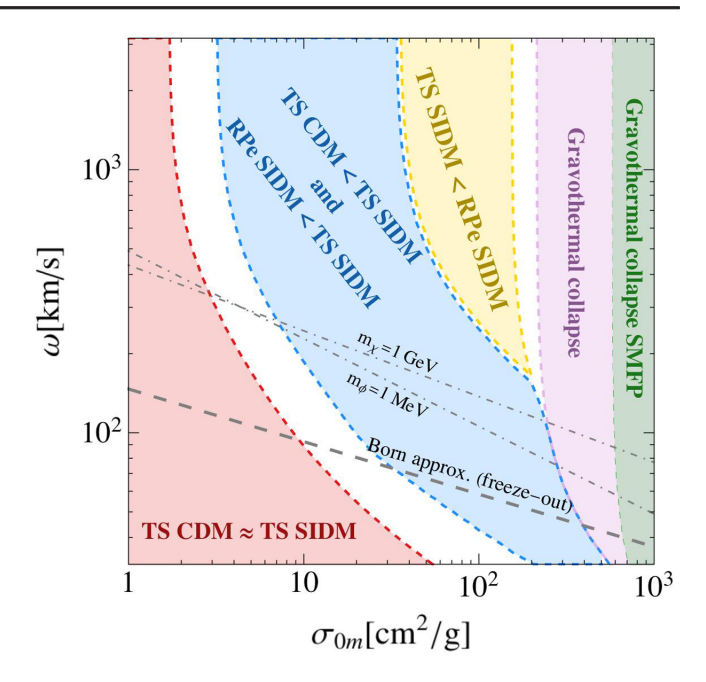


FIG. 2. Schematic diagram showing regions in SIDM parameter space where particular effects dominate in affecting a satellite's mass-loss evolution within the initial mass range $m_{\rm init} \in [10^9, 10^{10}] M_{\odot}$ and for the orbital parameters as in the $r_{\rm peri} \approx 20$ kpc examples in Fig. 1. White regions indicate parameters where not all satellites in the mass range fall into a given category. In the red region, there is little observable difference in mass loss between CDM versus SIDM. In the blue region tidal stripping (TS) is more effective in SIDM than in CDM, causing faster mass removal from the outskirts of SIDM satellites. In the vellow region, ram-pressure evaporation dominates over tidal stripping for SIDM satellites, causing efficient mass removal from central regions. In the pink and green regions, gravothermal collapse becomes relevant either in the long or short mean free path regimes for isolated satellites; to the left of these regions, the collapse timescale can be reduced due to tidal stripping. Also shown in gray are curves relevant for a dark sector populated by thermal freeze-out of $\chi\chi\to\phi\phi$. Above the dashed curve, the Born approximation holds for a scenario where α_D is fixed to give the correct dark matter thermal abundance. The dot-dashed curves correspond to example values for m_{γ} and m_{ϕ} .

corresponds to the best-fit concentration-mass relation of Ref. [53] at z=1 under the assumption that this relation approximately holds for SIDM cross sections considered in this study (see Ref. [54] and discussion in the Appendix B). The comparison between SIDM and CDM is done by averaging the mass loss over the last 2.5 of 7 Gyr orbits.

In the red region, the ratio of mass loss between SIDM and CDM is less than 5% and little difference is expected in satellite distributions. In the blue region, tidal stripping removes more mass from an SIDM satellite than from its CDM counterpart. Here, ram-pressure evaporation is small and therefore most mass is lost on the outskirts of the satellite. In the yellow region, ram-pressure evaporation in SIDM dominates over tidal stripping, and significant mass

loss is expected from the centers of SIDM satellites. These results differ from those in Ref. [13], which found that satellites are preferentially destroyed in SIDM halos solely because of ram pressure. This could potentially be explained by the fact that Ref. [13] used DM-only simulations with cored hosts (that have ~35% less mass below ~10 kpc compared to their CDM counterpart), thereby reducing the effects of tidal stripping for satellites with small enough pericenters.

In the pink region, the gravothermal collapse timescale for an isolated halo is short, $t_{\rm GC} < 10$ Gyr. The green region within the pink denotes parameters for which the MFP is shorter than the Jeans length of the core and collapse occurs in the rapid SMFP regime. In both, tidal stripping and ram-pressure evaporation remain active, but calculating their effects requires accounting for the initially collapsed halo. A caveat to this is that, even to the left of the pink region, where $t_{\rm GC}$ for an isolated halo is long, tidal stripping can significantly decrease its value. Therefore, the pink region should be thought of as parameters where LMFP gravothermal collapse can occur for isolated satellites before infall or with large pericenters.

A version of Fig. 2 including the effects of a point mass of $10^{11} M_{\odot}$ (a proxy for the MW's stellar disk) is available in Appendix C, Fig. 8. We find that the addition of this mass changes the results of the figure by a small amount, mostly increasing the area of the blue region and decreasing the area of the red region.

C. Constraints from dwarf galaxy measurements

A clear understanding of the orbital effects that dominate for different σ_{0m} and ω is critical for testing SIDM. We provide a proof-of-concept example of how to perform such tests by using the central density of the Draco dwarf galaxy (Fig. 3), as well as those of Ursa Minor, Segue 1, and Tucana 2 (Fig. 4). These constraints rely on each dwarf's central density measurement, which are provided in Table I.

There are two constraints that can be obtained using dwarf galaxies with particularly high central densities. The first ("isothermal-coring constraint") arises when self-interactions reduce the central density of the dwarf galaxy too much in a region of parameter space where gravothermal collapse is not possible. The second ("ram-pressure constraint") is a bound that arises from the potential of ram-pressure evaporation to remove too much mass from the interior of the dwarf galaxy. Precise details of how these constraints are conservatively placed are provided in Appendix B.

The first bound, shown as the leftmost dark blue region in Fig. 3, arises from the requirement that heating of the core not reduce Draco's present-day central density (at 150 pc) ρ_{150} by more than 2σ below its measured value [11]. To obtain a conservative estimate of this bound, we marginalize over the unknown present-day mass of

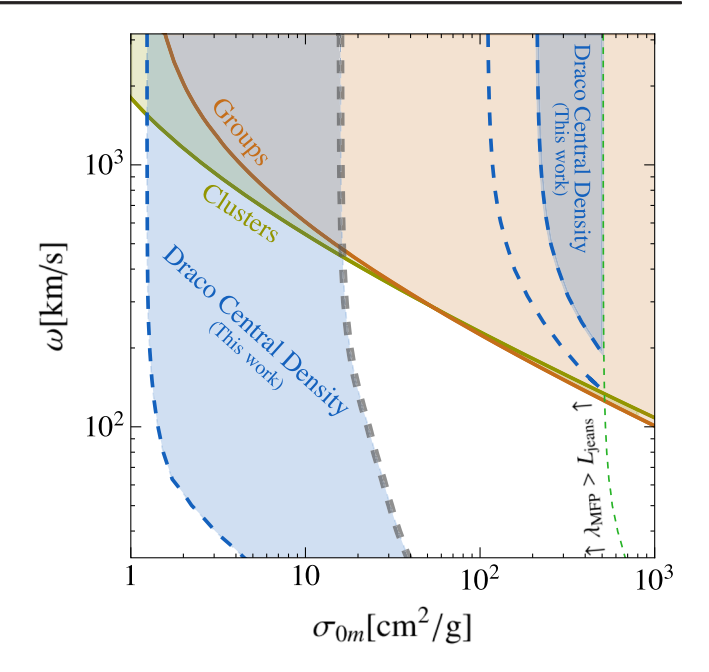


FIG. 3. Conservative constraints based on measurements of Draco's central density, which arise from overcoring of an isothermal SIDM profile (leftmost dark blue region) and excessive mass removal from ram-pressure evaporation (rightmost dark blue region), shown for the 2σ lower limit on the measurement of ρ_{150} for Draco. Also shown are existing 95% confidence-level bounds from galaxy groups (brown) and clusters (yellow) [55].

Draco by choosing the value that gives the largest central density at every point in parameter space. We also take the 2σ upper limit for Draco's concentration at z=1, which corresponds to the weakest constraint; we have verified that choosing a larger redshift produces a less conservative result. Finally, we require that $t_{\rm GC}$ is too long for gravothermal collapse to be active, even when tidal stripping effects are included. In the limit of constant interaction cross section, these results are consistent with Ref. [8], albeit slightly weaker due to our conservative assumptions. A careful understanding of the role of gravothermal collapse in this region of parameter space enables us to extend the bounds to lower velocity scales compared to Ref. [8].

The second bound, shown as the rightmost dark blue region in Fig. 3, arises in regimes where ram-pressure evaporation removes too much mass from the central regions of Draco during its most recent pericentric passage. Draco's orbit is calculated from its measured position and velocity [60]. To conservatively estimate the bound, an initially fully gravothermally collapsed halo is taken, with a core radius that gives the maximal possible density at 150 pc, where Draco's density is measured. The inner (outer) dashed curves correspond to the 1σ lower (upper) limit on the MW mass, $M_{\rm MW} = (1.3 \pm 0.3) \times 10^{12} M_{\odot}$ [61]. It should be noted that there are additional uncertainties (of

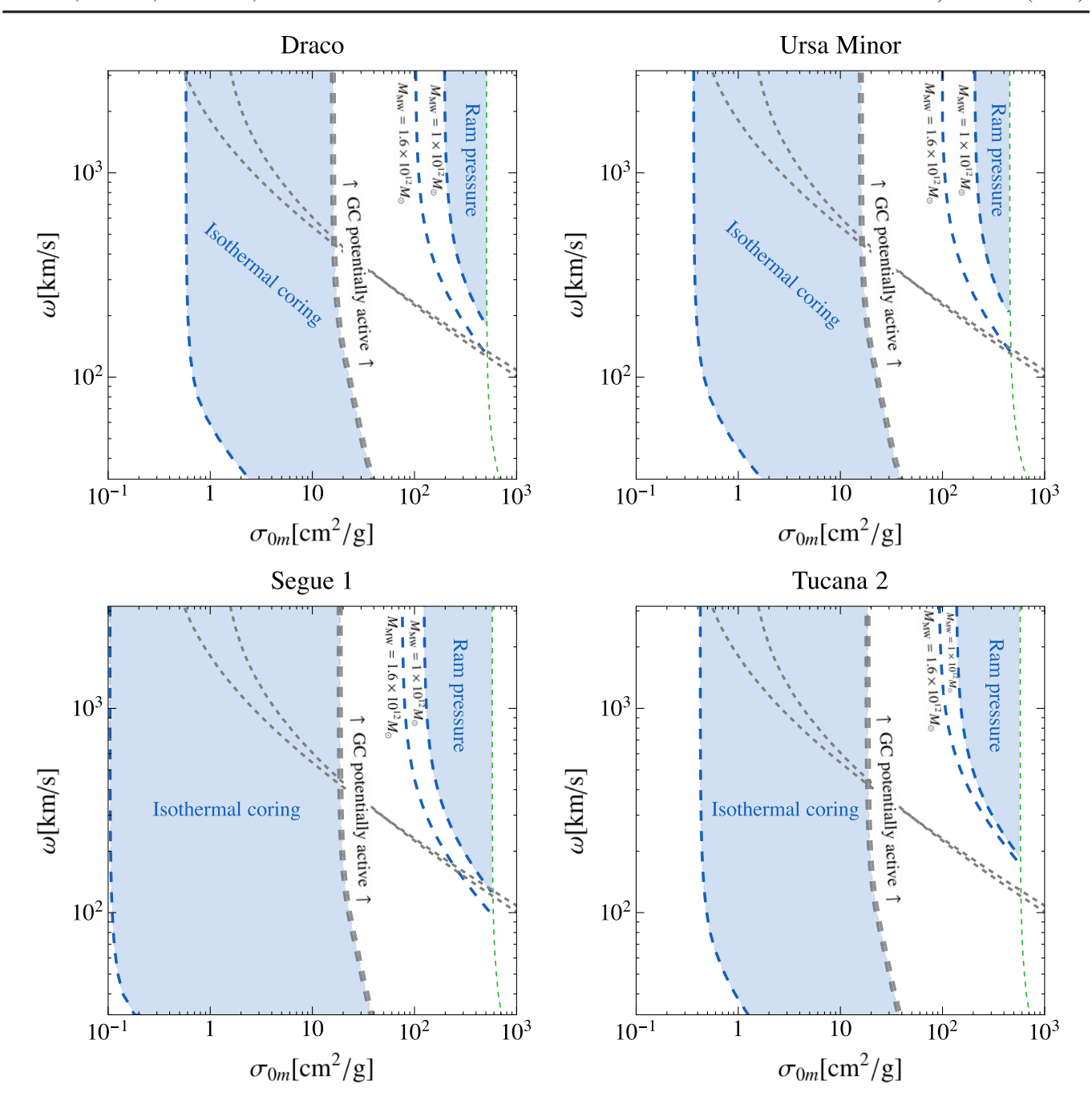


FIG. 4. Constraints similar to those of Fig. 3 for three additional systems: the classical dwarf Ursa Minor and the ultrafaint dwarfs Segue 1 and Tucana 2. For completeness, the Draco bound is shown here as well. For these constraints, the 1σ lower limit on measurements of ρ_{150} or $\bar{\rho}_{1/2}$ are used. Note that the Draco bound shown here takes the 1σ lower limit on the measured ρ_{150} , whereas that in Fig. 3 takes the 2σ lower limit. Also shown in dashed gray are existing 95% confidence-level bounds from galaxy groups and clusters [55].

similar order) associated with the orbit of Draco and other MW satellites [2,60]. Better measurements of the orbital parameters would thus allow for a more robust constraint. We only evolve the satellite for one orbital period in order to avoid complications such as changes in the orbit induced by the Large Magellanic Cloud (LMC) or by time dependence of the MW's potential; allowing for two full orbits

results in stronger bounds that happen to closely track the outer dashed curve. It is likely that a full analysis will result in ruling out additional high σ_{0m} regions, however, our analysis also reveals that core collapse can insulate against that possibility. We note that the ram-pressure bound falls within a parameter space region that is anyway constrained by galaxy groups and clusters [55].

The conservative bounds presented in this study identify regions of SIDM parameter space where a dedicated analysis of all MW dwarfs should have excellent sensitivity. Indeed, we have derived bounds using Ursa Minor, Segue 1, and Tucana 2, which are all consistent with each other and shown in Fig. 4. For these results, we have used the 1σ lower limits on measurements of ρ_{150} for Draco and Ursa Minor and of $\bar{\rho}_{1/2}$ (the average central density within the half-light radius of the galaxy) for Segue 1 and Tucana 2. The choice of 1σ , as opposed to the 2σ lower limit used for the Draco bound in the main text, illustrates the strong sensitivity of the isothermal coring bound to this choice. This sensitivity is due to the fact that central densities of an isothermal cored profile change slowly as σ_{0m} is varied. The ram-pressure bounds are much less sensitive to small variations in the measurement of ρ_{150} or $\bar{\rho}_{1/2}$.

Figure 3 also shows bounds from groups and clusters [55]. There exist comparable bounds from oscillations of brightest cluster galaxies [62] and a tighter bound from a strong lensing analysis in cluster galaxies [63] with possible connections to core collapse [64–66]. Combined with the cluster and group bounds, our results favor either a velocity-dependent SIDM cross section that can trigger core collapse or small cross sections which more closely resemble CDM.

IV. CONCLUSIONS

This study provides quantitative and intuitive understanding of the SIDM physics that affects internal properties and distributions of satellites within a MW-like host. The orbits of satellites with given initial masses, concentrations, and eccentricities were compared for different velocity-dependent, anisotropic cross sections. This semi-analytical approach is beneficial for identifying the physical mechanisms that affect satellite orbits in different regions of SIDM parameter space and should hold so long as satellites are not significantly deformed along their orbits.

We identified several key regimes of interest in SIDM parameter space where particular mechanisms affect satellite orbits. Additionally, we placed conservative constraints on SIDM parameter space using measured central densities of Draco, Ursa Minor, Segue 1, and Tucana 2, which all provided consistent results. When combined with existing constraints, our findings strongly argue for SIDM models where velocity-dependent interactions can trigger gravothermal collapse in at least some satellites. We find that models with small cross sections are also allowed by our restricted analysis of the MW satellites. However, these models are essentially collisionless and we would categorize them as CDM rather than SIDM.

The results of this work underscore how individual MW satellites can provide remarkable sensitivity to velocity-dependent DM self-interactions. We also anticipate that the mass-loss and gravothermal collapse mechanisms studied

here may translate into potentially observable differences in the population statistics of satellites. With the abundance of observational data rapidly becoming available for both the MW and other MW-like systems in the Local Group, satellite galaxies will provide a critical—and potentially definitive—exploration of the SIDM parameter space.

ACKNOWLEDGMENTS

The authors gratefully acknowledge S. Carlsten, J. Greene, E. Nadler, and P. Natarajan for useful conversations. F. J. is supported by the Troesh Scholarship at Caltech. M. K. is supported by the NSF under Grant No. 1915005. M. L. and O. S. are supported by the DOE under Award No. DE-SC0007968 and the Binational Science Foundation (Grant No. 2018140). O. S. is also supported by the NSF (Grant No. PHY-1915409).

APPENDIX A: DETAILED PROCEDURE FOR SATELLITE ORBIT MODELING

As discussed in the main text, there are three key ingredients required to model a satellite's orbit in both the CDM and SIDM cases. This appendix explores these ingredients in detail, focusing on (a) the density profiles of the satellite and host halos, (b) the formalism for describing satellite mass loss from tidal stripping and ram-pressure evaporation, and (c) the numerical method for solving the equation of motion of the satellite.

We note that the modeling described below is meant to capture only qualitative behavior of a satellite galaxy orbiting a massive host. In particular, details such as tidal tracks [67], effects related to shocking [68], and effects of the host's stellar content [20] are not incorporated in our modeling. Additionally, our modeling does not account for mass evolution of the host under the assumption that this effect is small for the case of the Milky Way [69]. While such effects could change quantitative results, the specific changes to the constraints of Figs. 3 and 4 serve to shift curves toward constraining more parameter space (or moving them by a negligible amount) and therefore our results remain conservative.

1. Host and satellite density profiles

The density profile for a CDM satellite or host, as well as for a baryon-dominated SIDM host, is taken to be an NFW profile [43]. The enclosed mass of this profile has the form

$$M_{\rm NFW}(r) = 4\pi \rho_0 r_s^3 \left[\ln \left(\frac{r + r_s}{r_s} \right) - \frac{r}{r + r_s} \right], \quad (A1)$$

where r_s is the scale radius and ρ_0 is a normalization density. SIDM satellite profiles that are not gravothermally collapsed are modeled as Eq. (2). The density distributions corresponding to Eqs. (A1) and (2) can be found by differentiating the formula for the enclosed mass and are

initially truncated at the virial radius. For the SIDM profile, the core density is $3/2 \times \rho_0 r_s/r_c$.

Once the virial mass M_{200} of the halo is specified, its virial radius is determined by requiring that the average halo density is 200 times the critical density, $\rho_{\rm crit}(z)$. The NFW scale radius then follows from the concentrationmass relation in Ref. [53] (which also agrees with the relations found in Refs. [70,71]), with ρ_0 obtained by requiring that the enclosed mass at r_{200} gives M_{200} . Although the concentration-mass relation was derived for CDM, we assume that this relation approximately holds or that possible variations to it do not have a large effect for SIDM cross sections considered in this study. Below $\sim 1 \text{ cm}^2/\text{g}$, this has been verified in simulations [54]. At cross sections which are much larger (of order 30 cm²/g and above) but below values for which gravothermal collapse occurs, core sizes could potentially be modified by such effects. Unless otherwise specified, the concentration of the satellite galaxy is evaluated at redshift z = 1, corresponding to the time of infall in our examples. Note that, for the host halo specifically, we take a concentration of $c_{200} = 10$ and assume a total mass of $10^{12} M_{\odot}$ at time of satellite infall, unless otherwise specified. For the case of an NFW profile, this procedure is all that is required to set the free parameters of the halo model. For the SIDM profile, this procedure sets the properties of the NFW profile before self-interactions heat the central regions of the halo and the core forms. During this process, some DM will be pushed out from the innermost region of the halo. We have verified using idealized N-body SIDM simulations and cosmological FIRE-SIDM simulations [72] that the original NFW profile provides a good description beyond r_c .

The value of the radius r_1 is approximated using the following equation:

$$\langle \sigma_m v \rangle \rho_{\text{SIDM}}(r_1) t_{\text{age}} = 1,$$
 (A2)

where $t_{\rm age}$ is the age of the satellite. The velocity-averaged transfer cross section $\langle \sigma_m v \rangle$ is given by

$$\langle \sigma_m v \rangle = \frac{1}{m_{\chi}} \int f(\mathbf{v}_1) f(\mathbf{v}_2) v \frac{d\sigma}{d\theta} (1 - \cos\theta) d^3 \mathbf{v}_1 d^3 \mathbf{v}_2 d\theta,$$
(A3)

where $\mathbf{v} \equiv \mathbf{v}_1 - \mathbf{v}_2$ is the relative velocity, and θ is the scattering angle. This can be simplified to a single integral over v. Note that the $1 - \cos \theta$ weighting does not suppress contributions from scattering events where the two particles exchange velocities ($\theta \simeq \pi$), which would not change the halo density profile. To take this into account, other weights such as $\sin^2 \theta$ (viscosity cross section) [73] or $(1 - |\cos \theta|)$ [74,75] have been proposed. Importantly, all variations should reproduce the same $\langle \sigma_m v \rangle$ for values of ω

much larger than the typical velocity dispersion of the satellite [up to $\mathcal{O}(1)$ factors]. Therefore, any such variations will have small effects on our results since satellites have typical dispersions of $\mathcal{O}(10)$ km/s, while we have considered $\omega \gtrsim 30$ km/s. The $(1-|\cos\theta|)$ weighted cross section is about a factor of 2 smaller for w larger than the dispersion of DM, while for small w the differences are 20%-30%. The $\sin^2\theta$ weighted cross section is different from the $1-\cos(\theta)$ by 33% or less, depending on the value of w. This O(1) systematic, which should be kept in mind when interpreting our results, should be resolved in the future with more simulations covering a range of w values.

In the equation above, $f(\mathbf{v})$ is the Maxwell-Boltzmann velocity distribution for the DM,

$$f(\mathbf{v}) = \left(\frac{3}{2\pi\sigma_{\rm v}^2}\right)^{3/2} e^{-3\mathbf{v}^2/2\sigma_{\rm v}^2} \tag{A4}$$

and $\sigma_{\rm v}$ is the root-mean-square velocity dispersion. Assuming an isotropic velocity distribution, then $\sigma_{\rm v}^2 = 3\sigma_r^2$, where the radial dispersion σ_r follows from the radial Jeans equation,

$$\sigma_r^2(r) = \frac{1}{\rho_{\text{SIDM}}(r)} \int_r^{\infty} \frac{\rho_{\text{SIDM}}(r')v^2(r')}{r'} dr', \quad (A5)$$

with $v^2(r) = GM_{\rm SIDM}(r)/r$. With r_1 obtained in the way detailed above, we find that using $r_c = 0.5r_1$ in Eq. (2) provides an accurate fit to the SIDM profile obtained from isothermal Jeans modeling or from idealized SIDM N-body simulations. For cross sections of $\sigma_m = 1-20$ cm²/g and for $t_{\rm age} = 1-10$ Gyr, Eq. (2) with $r_c = 0.5r_1$ agrees with simulation results to percent level. For larger cross sections that yield $r_1 > r_s$, we find that setting $r_c = r_s$ provides better fits.

For certain ranges of parameter space, gravothermal collapse can affect the density distribution of SIDM halos and Eq. (2) no longer suffices. Gravothermally collapsed profiles in the LMFP regime are modeled based on the results of numerically solving for the self-similar solution in Ref. [32]. In this regime, the solution for the gravothermally collapsing region and its surroundings takes the form of a flat core within a shrinking radius r_c . Above this radius, the density decreases as $\rho_{\rm GC} \propto r^{-2.19}$ before transitioning to $\rho_{NFW}(r)$ above the radius $r \gtrsim r_{GC}$. This scenario is modeled by the profile given in Eq. (3). This profile decreases as r^{-3} when $r \gg r_{\rm GC}$, as $r^{-2.19}$ when $r_c <$ $r < r_{\rm GC}$ and flattens out when $r < r_{\rm c}$, as would be expected from a collapsing core in the LMFP regime. We have verified that this density model is qualitatively similar to what was found in SIDM simulations with collapsing halos [31,36]. Note, however, that Ref. [14] finds a steeper single power-law profile in the region outside the core of r^{-3} for satellites deep in the core-collapse phase. Such a change to the profile would mildly effect the ram-pressure bounds in Figs. 3 and 4.

2. Mass loss

Satellite mass is lost in one of two ways. For both SIDM and CDM scenarios, tidal stripping can remove mass from the outskirts of the satellite. The tidal stripping mass-loss rate is given by Eq. (5). The tidal radius ℓ_t is calculated with Eq. (4), with g(r) now written explicitly [48,49],

$$\mathscr{C}_t \simeq r \left[\frac{m_{\text{sat}}(\mathscr{C}_t) / M_{\text{host}}(r)}{2 - \frac{d \ln M_{\text{host}}}{d \ln r} + \frac{v_{\text{tan}}^2(r)}{v_{\text{circ}}^2(r)}} \right]^{1/3}, \tag{A6}$$

where $v_{\rm tan}(r) = |\hat{r} \times \mathbf{v}_{\rm sat}|$ is the instantaneous tangential velocity of the satellite and $v_{\rm circ}(r) = \sqrt{GM_{\rm host}(r)/r^2}$ is its circular velocity. The dynamical time is taken to be

$$t_{\rm dyn}(r) = \sqrt{\frac{3\pi}{16G\bar{\rho}_{\rm host}(r)}},\tag{A7}$$

where $\bar{\rho}_{\text{host}}$ is the average density of the host within radius r [51].

For SIDM satellites only, ram-pressure evaporation can remove mass from all regions of the satellite. Ram-pressure evaporation is calculated according to Eq. (6), with the evaporation fraction given by

$$\eta_e = \frac{1}{\sigma} \int_{\pi - \theta_{\rm crit}}^{\theta_{\rm crit}} \frac{d\sigma}{d\theta} d\theta, \quad \text{where } \theta_{\rm crit} = \arccos\left(\frac{x^2 - 1}{x^2 + 1}\right)$$
(A8)

and $x=\bar{v}_{\rm esc}/v_{\rm sat}$ with $\bar{v}_{\rm esc}$ the average escape velocity of the satellite. The cross section σ_m in Eq. (6) is evaluated at a velocity equal to the satellite's velocity with respect to the host plus the average escape velocity of the satellite, $v=v_{\rm sat}+\bar{v}_{\rm esc}$ [30]. The latter is a reasonable approximation because host-satellite scattering events typically occur close to the center of the satellite. In general, $\bar{v}_{\rm esc}/v_{\rm sat}\ll 1$ for the cases of interest here, so this approximation is sufficient even for scatterings that occur in the outer regions of the satellite.

Knowing both the mass-loss rate from tidal stripping and ram-pressure evaporation through Eqs. (5) and (6), a prescription can be established to track the total mass and density profile of the satellite along its orbit. For any small time step $\Delta t = t' - t$, the tidal stripping or ram-pressure evaporation mass loss can be evaluated by

$$\Delta m_{\rm TS/RPE} = \int_{t}^{t'} \dot{m}_{\rm TS/RPE} dt, \tag{A9}$$

where $\Delta m_{\rm TS/RPE}$ are typically negative.

Any mass that is removed via tidal stripping is taken away from the outermost region of the satellite halo. This is modeled by defining a truncation radius that evolves over time. At a given time step, the truncation radius is taken to decrease from r_{trunc} to r'_{trunc} such that the mass enclosed between these radii is equal to Δm_{TS} , namely,

$$M(\rho_0, r'_{\text{trunc}}) - M(\rho_0, r_{\text{trunc}}) = \Delta m_{\text{TS}}.$$
 (A10)

In contrast, mass that is removed via ram-pressure evaporation is taken from all regions of the satellite by changing the normalization of its density profile. This prescription removes mass from regions of the halo in a fashion that is linearly proportional to the local density at any given point. The normalization is taken to change from ρ_0 to ρ_0' such that the mass difference is equal to $\Delta m_{\rm RPE}$, namely,

$$M(\rho'_0, r_{\text{trunc}}) - M(\rho_0, r_{\text{trunc}}) = \Delta m_{\text{RPE}}.$$
 (A11)

If the velocity of the satellite is anomalously small, then $\Delta m_{\rm RPE}$ can be positive, i.e., the satellite accretes mass. Although this is possible, it is never the case for the scenarios considered in this study.

3. Orbits

The evolution of the satellite's orbit is obtained by solving the equation of motion, Eq. (7). The dynamical friction is modeled using the Chandrasekhar formula [52],

$$\mathbf{a}_{\mathrm{DF}} = -4\pi G^{2} m_{\mathrm{sat}} \rho_{\mathrm{host}} \ln \Lambda F_{\mathrm{v}}(v_{\mathrm{sat}}) \frac{\mathbf{v}_{\mathrm{sat}}}{v_{\mathrm{sat}}^{3}}, \quad (\mathrm{A}12)$$

where the Coulomb logarithm is defined as $\ln \Lambda = \min[s,1] \ln (M_{\text{host}}/m_{\text{sat}})$ and is calibrated to simulations [47,76], with $s=(3r+r_{s,\text{host}})/(r+r_{s,\text{host}})$ and $r_{s,\text{host}}$ the scale radius of the host [51]. Assuming an isotropic and Maxwellian host halo, then $F_{\text{v}}(v_{\text{sat}})=\text{erf}(y)-2ye^{-y^2}/\sqrt{\pi}$ with $y=v_{\text{sat}}/(\sqrt{2}\sigma_{\text{r}})$, where σ_r is the radial velocity dispersion of the host.

Ram-pressure deceleration, calculated according to Eq. (8), can affect a satellite's orbit, especially in regions of large self-interaction cross sections. For $v_{\rm sat}\gg v_{\rm esc}$, the deceleration fraction η_d is

$$\eta_d = \frac{1}{m_\chi v \sigma} \int \Delta p_z \frac{d\sigma}{d\theta} d\theta \approx \frac{1}{2} \left(\frac{v_{\rm esc}}{v_{\rm sat}} \right)^2, \quad (A13)$$

where Δp_z is the change in momentum along the direction of motion of the incoming particles. The velocity dispersion $v_{\rm disp}$ of interacting particles causes a further suppression of η_d when $v_{\rm sat} \lesssim v_{\rm disp}$. However, at pericenter (when the effect is largest) the satellite's velocity is larger than the dispersions of both satellite and host, and the suppression does not enter the calculation. Figure 5 compares the role of ram-pressure deceleration to that of dynamical friction. The

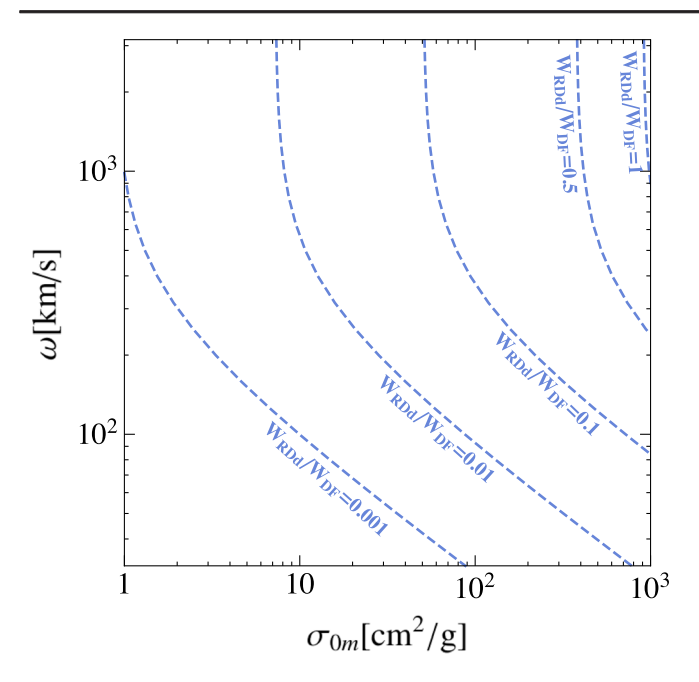


FIG. 5. Contours of the ratio of work done by ram-pressure deceleration to the work done by dynamical friction over 7 Gyr orbits for $m_{\rm init} = 10^{10.5} M_{\odot}$ (the result is very weakly dependent on $m_{\rm init}$) and a $10^{12} M_{\odot}$ host. In most of the parameter space, rampressure deceleration plays a subdominant role in the orbital evolution of satellites.

contours denote constant values of the ratio of work done by ram pressure to that done by dynamical friction $W_{\rm RPd}/W_{\rm DF}$ over 7 Gyr orbits for a $m_{\rm init}=10^{10.5}M_{\odot}$ satellite orbiting a $10^{12}M_{\odot}$ host. For most of the parameter space considered, orbital decay from ram-pressure deceleration is highly subdominant to the effects of dynamical friction and only for the largest cross sections considered do the two forces produce comparable work. Although the result is plotted only for a single satellite mass in Fig. 5, the ratio $W_{\rm RPd}/W_{\rm DF}$ is only mildly dependent on $m_{\rm init}$. This occurs because of a cancellation between the explicit mass dependence of the dynamical friction force and the mass dependence of the satellite's escape velocity, which enters the ram-pressure calculation.

To evaluate the equation of motion Eq. (7), one must specify the initial conditions of the problem. In our case, these are (a) the virial mass of the host halo, which sets the NFW density profile through the concentration relation, and (b) the initial density profile, position, and velocity of the satellite. Additionally, one must specify the SIDM parameters $\{\sigma_{0m}, \omega\}$. The density profile of the host galaxy is assumed to follow an NFW profile in all cases. For the satellite, the initial profile depends on whether one is considering a CDM, isothermally cored SIDM, or a gravothermally collapsing scenario. For the case of CDM, one need only specify the mass of the halo, the scale radius is then set through the concentration-mass relation. For the isothermal cored SIDM scenario, after specifying the mass

and calculating the scale radius, one must also specify $t_{\rm age}$, which sets r_1 through Eq. (A2). In this study, we always take $t_{\rm age} = 10$ Gyr; this assumption is only relevant when r_c has not yet saturated r_s , which only occurs when $\sigma_{0m} \lesssim 20 \text{ cm}^2/\text{g}$ for the range of masses considered in this study.

After having specified these values, the evolution time is divided into small time steps such that $\Delta t \ll t_{\rm dyn}$ and slightly larger time steps $\Delta T = (20-30)\Delta t$. At each Δt interval, $\Delta m_{\rm TS}$ and $\Delta m_{\rm RPE}$ are calculated and $r_{\rm trunc}$ and ρ_0 are updated accordingly. The orbit is reevaluated for every ΔT interval using Eq. (7), taking the masses, density profiles, positions, and velocities from the end of the previous interval as the initial conditions. The larger ΔT interval is introduced for computational simplicity. We verify that the intervals are always small enough to have a negligible effect on the results. The final result of the calculation is the mass, density profile, position, and velocity of the satellite at all times. Additionally, one can sum over $\Delta m_{\rm TS}$ and $\Delta m_{\rm RPE}$ to evaluate the total mass lost to tidal stripping and ram-pressure evaporation and perform integrals over the dynamical friction and ram-pressure deceleration to calculate the work done by these forces.

APPENDIX B: CONSTRAINTS FROM CENTRAL DENSITIES OF DWARF GALAXIES

This appendix reviews in detail how to obtain conservative SIDM constraints using the central density of the Draco dwarf (Fig. 3) and the additional results for Ursa Minor, Segue 1, and Tucana 2 (Fig. 4). These constraints rely on present-day measurements of each dwarf's central density, which are provided in Table I. Note that for Draco and Ursa Minor, we use ρ_{150} , defined as the density at 150 pc. For Segue 1 and Tucana 2, we use the average central density $\bar{\rho}_{1/2}$ within $r_{1/2}$, the radius within which half of the galaxy's stellar luminosity is enclosed

TABLE I. The central densities for Draco and Ursa Minor correspond to the 1σ lower limit on the measured ρ_{150} , and for Segue 1 and Tucana 2 correspond to the 1σ lower limit on the measured $\bar{\rho}_{1/2}$. Note that in the main text the Draco bound corresponds to the 2σ lower limit. Also note that for Draco and Ursa Minor, we use ρ_{150} , defined as the density at 150 pc. For Segue 1 and Tucana 2, we use the average central density $\bar{\rho}_{1/2}$ within $r_{1/2}$, the radius within which half of the galaxy's stellar luminosity is enclosed ($r_{1/2}=36$ pc for Segue 1 [56] and $r_{1/2}=165$ pc for Tucana 2 [57]). We use the concentration-mass relation from Ref. [53]. M_{200} is the infall mass at z=1.

Dwarf galaxy	Central density $(10^7 M_{\odot} \text{ kpc}^{-3})$	$M_{200}~(M_{\odot})$	$c_{200}(z=1)$
Draco	16.65 [11]	1.8×10^9 [58]	8.84 ± 3.36
Ursa Minor	19.80 [11]	2.8×10^9 [58]	8.56 ± 3.25
Segue 1	92.71 [56]	$10^9 [59]$	9.24 ± 3.52
Tucana 2	21.20 [57]	$10^9 [59]$	9.24 ± 3.52

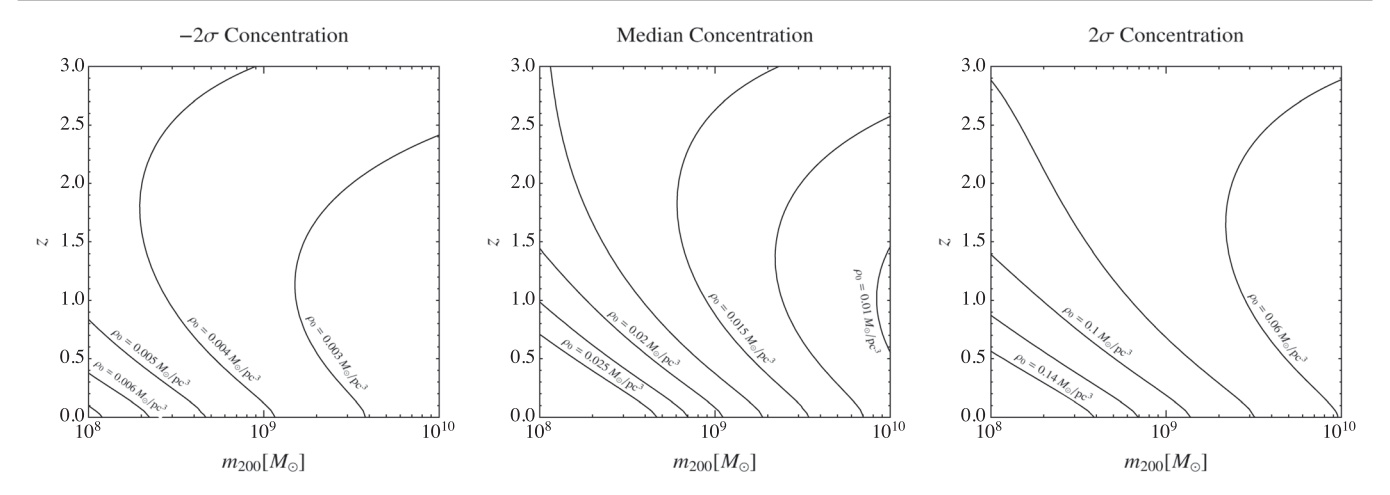


FIG. 6. NFW profile scale densities as a function of z and m_{200} for varying distance from the median concentration-mass relation of Ref. [53]. In all panels, the central density increases, or is approximately constant, with decreasing z for $z \lesssim 2$. Note that c_{200} is a function of both z and m_{200} .

 $(r_{1/2} = 36 \text{ pc for Segue 1 [56] and } r_{1/2} = 165 \text{ pc for Tucana 2 [57]}).$

The goal of this procedure is to estimate the potential of dwarf observations in constraining SIDM parameter space. Our approach is to make very conservative choices when it comes to assumptions that feed into the central density prediction. As already highlighted in the main text, the results of this exercise demonstrate the important role played by Milky Way dwarfs in constraining σ_{0m} and ω . This motivates pursuing a more rigorous likelihood procedure in future work. For example, the conservative constraints presented in this work can be improved by performing a full Bayesian analysis that accounts for the unknown parameters with well-motivated priors and appropriately stacks the contribution of each dwarf in the likelihood procedure.

As discussed in the main text, there are two types of constraints that can be obtained: a ram-pressure constraint and an isothermal-coring constraint.

1. Ram-pressure constraint

To evaluate the impact of ram-pressure evaporation on any given dwarf, we infer its density and concentration at infall and initialize its energy and angular momentum given present-day observations of the system and the central density profile of the Milky Way. The orbit is then evolved forward in time. Specifically:

(1) The infall mass of each satellite M_{200} is provided in Table I. For the classical dwarfs, Draco and Ursa Minor, the infall masses are taken from Ref. [58]. These infall masses are inferred from abundance matching with mean star formation rates. For the ultrafaint dwarfs, Segue 1 and Tucana 2, the infall masses are taken to be $10^9 M_{\odot}$, based on the approximate upper limit of high resolution cosmological simulations with low stellar content [59].

- We assume here that infall properties and star formation physics are not significantly modified by self-interactions, but this remains to be tested with simulations.
- (2) The initial density distribution for the satellite is taken to be a fully gravothermally collapsed profile following Eq. (3). Importantly, gravothermal collapse in the LMFP regime cannot create arbitrarily large densities at any given radius or arbitrarily large average densities within any given radius. Specifically, below some minimal value, any additional decrease in the core size will not affect ρ_{150} or $\bar{\rho}_{1/2}$ of the satellite. The value of r_c is chosen such that this maximal central density is achieved for each satellite. For Draco and Ursa Minor, $r_c = 50$ pc, for Segue 1, $r_c = 2$ pc, and for Tucana 2, $r_c = 20$ pc. These choices correspond to the largest possible initial conditions for the central density and are therefore maximally conservative.
- (3) The satellite's concentration c_{200} at time of infall is taken from the best-fit concentration-mass relation of Ref. [53]. We conservatively evaluate the concentration at z = 1. The star formation histories of Draco, Ursa Minor, Segue 1, and Tucana 2 suggest that their infall times may be closer to $z \sim 2$ [77,78]. We have verified that increasing the infall redshift decreases the initial central density of an NFW profile and would thus strengthen the constraints. Figure 6 shows this explicitly; we plot the NFW profile scale density for varying values of halo mass, redshift, and distance from the median concentration-mass relation of Ref. [53]. We note that, while concentration-mass relation of Ref. [53] agrees with Refs. [70,71], it differs from Ref. [79], and this is a potential caveat to the arguments made above.
- (4) The scale radius of the satellite's halo is determined from its concentration and M_{200} , which sets the virial

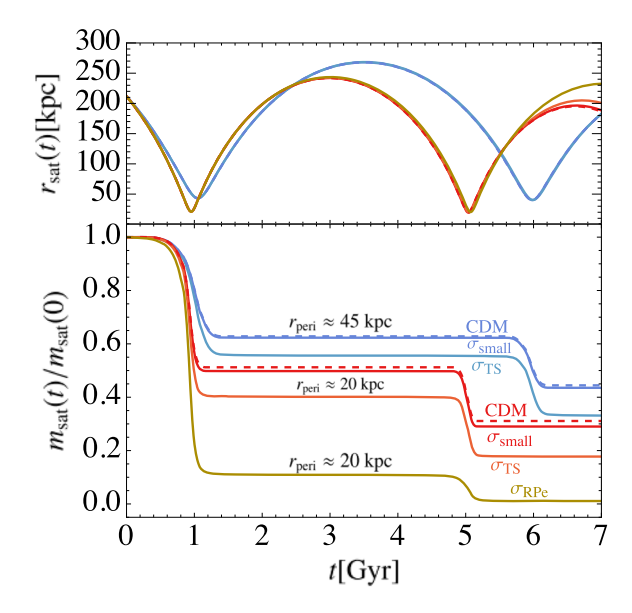


FIG. 7. Same as Fig. 1 (left) but with the addition of a point mass of $10^{11} M_{\odot}$ at the MW's center.

radius r_{200} through the critical density $\rho_{\rm crit}$. Additionally, the overall normalization of the density distribution ρ_0 is obtained by requiring that the enclosed mass at r_{200} gives the virial mass.

- (5) The satellite's energy and angular momentum at z=0 is estimated using its present-day velocity and position and the density profile of the Milky Way. The observations are taken from Ref. [60] for Draco, Ursa Minor, and Segue 1 and from Ref. [80] for Tucana 2. The resulting values of pericenters for each of the satellites are $r_{\rm peri} \approx 44$ kpc for Draco, $r_{\rm peri} \approx 46$ kpc for Ursa Minor, $r_{\rm peri} \approx 19$ kpc for Segue 1, and $r_{\rm peri} \approx 38$ kpc for Tucana 2, which are all slightly higher than the median estimates of Ref. [2] but within the 2σ error bands (smaller pericenters would correspond to slightly stronger constraints because ram-pressure evaporation would become more significant).
- (6) The satellite's orbit is obtained by placing it at some (arbitrary) initial position and evolving forward in time for one pericentric passage, using the approximate values for energy and angular momentum determined in the previous step. This procedure assumes that the energy and angular momentum of the satellite at infall match its present-day values and does not account for losses due to dynamical friction and ram-pressure deceleration. While these corrections are likely negligible for the $\mathcal{O}(10^9)M_{\odot}$ halos considered here, the choice of one pericentric passage minimizes the potential impact of these approximations. Additionally, the choice of a single pericentric passage avoids issues related to gravothermal collapse potentially occurring between passages. The constraints would significantly

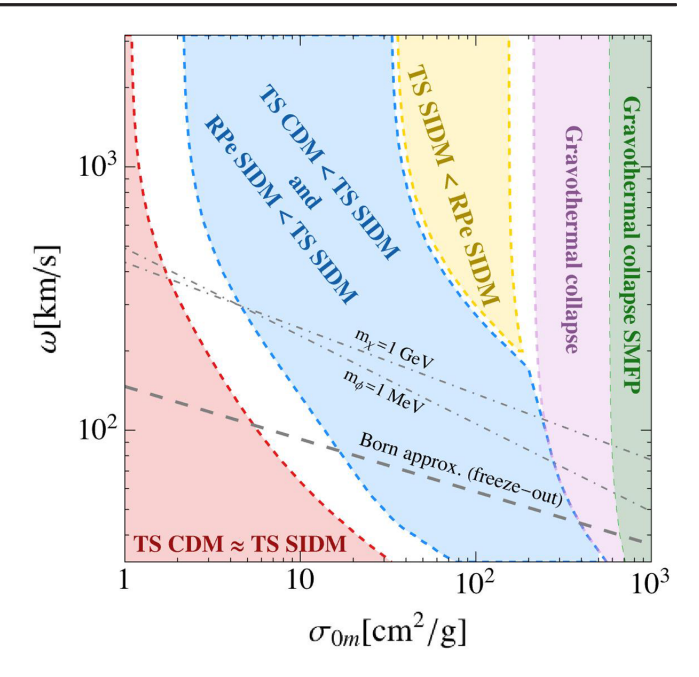


FIG. 8. Same as Fig. 2 but with the addition of a point mass of $10^{11} M_{\odot}$ at the MW's center.

strengthen the more pericentric passages are included, since more mass is removed from the satellite during each of these.

- (7) After evolving for a single orbit, the central density (either ρ_{150} or $\bar{\rho}_{1/2}$) is found and compared to the 2σ lower limit from observations for results shown in Fig. 3 and to the 1σ lower limit for results shown in Fig. 4. If the predicted value is larger than the observational lower limit, then the point in the $\{\sigma_{0m}, \omega\}$ parameter space is excluded.
- (8) The calculation is performed for two different Milky Way masses, 1×10^{12} and $1.6 \times 10^{12} M_{\odot}$, which correspond to the lower and upper 1σ limits quoted in Ref. [61].

2. Isothermal-coring constraint

To evaluate the impact of isothermal coring on any given dwarf, we determine its density distribution at present day while requiring that gravothermal collapse has not yet occurred. Specifically:

- (1) The density profile of the satellite is modeled by Eq. (2). The halo is assumed to relax for $t_{\text{age}} = 10$ Gyr, which sets the value of r_1 following Eq. (A2).
- (2) The central density of the profile depends on its current mass $m_{\rm sat}$ and on the value of r_s . Because the current mass of the satellite is not well constrained, we evaluate the central density (either ρ_{150} or $\bar{\rho}_{1/2}$) for a grid of masses. For a given value of $m_{\rm sat}$, the concentration of the satellite is taken from the 2σ upper limit of the concentration-mass relation from

Ref. [53] at z = 1. Then, for every point in the $\{\sigma_{0m},\omega\}$ parameter space, we choose the value of $m_{\rm sat}$ for which the central density is largest, i.e., the bound is weakest. We find that this value of m_{sat} is always less than the infall masses quoted in Table I and is around $10^{7.8-8.8} M_{\odot}$ for the four satellites considered in this study. These correspond to conservative choices for the satellite mass and concentration. The resulting value of the central density is then compared to the 2σ lower limit from observations for results shown in Fig. 3 and to the 1σ lower limit for results shown in Fig. 4. If the predicted value is larger than the observational lower limit, then the point in the $\{\sigma_{0m}, \omega\}$ parameter space is excluded. This sets the leftmost contour of the isothermal-coring bound. An important point is that as the cross section increases, the core size increases only until it reaches its maximal value at around $r_c \approx r_s$. For larger cross sections, the central density no longer decreases but rather remains constant. Therefore, much of the excluded parameter space is constrained at the same confidence level.

(3) The rightmost contour of the isothermal-coring bound is set by the requirement that gravothermal collapse be inactive. Specifically, we estimate the gravothermal-collapse timescale t_{GC} using [32]

$$t_{\rm GC} \approx \frac{290}{\langle \sigma_m v \rangle \rho_{\rm core}},$$
 (B1)

and require that $t_{\rm GC} > 20$ Gyr. This choice accounts for potential shortening of t_{GC} through the effects of tidal stripping, based on the results of Ref. [36]. For the velocity average, the dispersion is taken to be $\sigma_r = 1.1 \times v_{\text{max}}/\sqrt{3}$, where v_{max} is the maximal circular velocity of the NFW profile at radius $r_{\rm max} > r_c$. This may be derived from the maximum dispersion for an NFW halo $\max(v_{\rm rms})$ using the Taylor-Navarro [81] phase-space density Q(r) = $\rho(r)/v_{\rm rms}(r)^3 = 0.3/(Gv_{\rm max}r_{\rm max}^2(r/r_s)^{-\eta})$ with $\eta \simeq 2$ [82]. The median radial dispersion to v_{max} ratio plotted in Ref. [83] provides similar values (but about 10% higher). In principle, the velocity average for this calculation should weight correctly for energy transfer and therefore has different powers of v in Eq. (A3) [84]. However, for the reasons stated above, such variations to the calculation only change the result by $\mathcal{O}(1)$ for $\omega \gg \sigma_r$. We have verified that for $\omega \lesssim \sigma_r$, and with the assumption of weighting the cross section by $(v \sin \theta)^2$, the value of t_{GC} increases such that constraints presented in this work are

In the timescale defined above, $\rho_{\rm core}$ is taken to be the central density of the isothermal cored SIDM

profile, which should be interpreted as the minimum core density in the evolution of the halo. Note that since $v \propto v_{\text{max}}$ and $\rho_{\text{core}} \propto \rho_0$, this timescale has the same dependence on the initial profile as that in Ref. [36]. However, the timescale used here is roughly a factor of 2 larger than that in Ref. [36], which can be traced back to the choice of the LMFP conductivity normalization used to get a fit to halo profiles for moderate cross sections $\lesssim 10 \text{ cm}^2/\text{g}$. The formula used here for t_{GC} is more consistent with the evolution of the core density for large cross sections [32,35]. We evaluate t_{GC} for a grid of masses in the range $m_{\rm sat} \in [10^7 M_{\odot}, M_{200}]$ for every point in the $\{\sigma_{0m},\omega\}$ parameter space. The constraints do not extend to points in parameter space where $t_{GC} > 20$ Gyr for any mass within this range.

The final results for the classical dwarfs Draco and Ursa Minor, as well as the ultrafaint dwarfs Segue 1 and Tucana 2, are provided in Figs. 3 and 4. The additional systems complement the result for Draco in a number of ways. First, Draco's orbit has been shown to potentially be affected by the LMC [60]. If this is the case, then a full analysis should include the effects of Draco's interactions with the halo of the LMC and also account for the three-body orbit, both of which are beyond the scope of this work. However, the same study shows that Ursa Minor, which has a similar central density to Draco, is far less affected by the LMC. Specifically, the pericenter of Ursa Minor's orbit is expected to change far less when accounting for the multibody orbit of the dwarf, LMC, and the Milky Way. Second, Segue 1 and Tucana 2 are more DM dominated than either Draco or Ursa Minor, and thus have a different set of observational systematics. Finally, it is possible that the large central densities of the objects considered in this study could be the result of anomalously high concentrations, beyond even the 2σ upper limit values used for results where gravothermal collapse does not occur (2σ was chosen specifically because we consider some of the densest known satellites of the Milky Way). If this is the case, the constraints would weaken. However, the combination of all four analyses illustrates the point that a future study of an ensemble of dwarfs will provide a robust constraint on the SIDM parameter space.

APPENDIX C: SUPPLEMENTAL FIGURES

This section provides supplemental figures discussed in the main text. These figures quantify the effects of a spherical potential mimicking the MW's stellar disk on the mass removal rates of satellite galaxies considered in this study. In particular, we reproduce Figs. 1 (left) and 2, now including a point mass of $10^{11}M_{\odot}$ (comfortably larger than the baryonic mass of the MW) at the MW's center. We find that, for the orbits considered in this study, the results change by about 10% or less of $m_{\rm sat}(0)$. The nonspherical

nature of the disk and the associated effects of tidal heating and shocking are missing in this treatment. When these effects are included, we expect that the central densities of SIDM halos (that are not in the gravothermal core-collapse phase) will be further lowered, thereby strengthening the bounds we have derived.

- [1] A. W. McConnachie, Astron. J. 144, 4 (2012).
- [2] T. K. Fritz, G. Battaglia, M. S. Pawlowski, N. Kallivayalil, R. van der Marel, S. T. Sohn, C. Brook, and G. Besla, Astron. Astrophys. 619, A103 (2018).
- [3] S. G. Carlsten, J. E. Greene, A. H. G. Peter, J. P. Greco, and R. L. Beaton, Astrophys. J. 902, 124 (2020).
- [4] Y.-Y. Mao, M. Geha, R. H. Wechsler, B. Weiner, E. J. Tollerud, E. O. Nadler, and N. Kallivayalil, Astrophys. J. 907, 85 (2021).
- [5] M. Vogelsberger, J. Zavala, and A. Loeb, Mon. Not. R. Astron. Soc. 423, 3740 (2012).
- [6] J. Zavala, M. Vogelsberger, and M. G. Walker, Mon. Not. R. Astron. Soc. 431, L20 (2013).
- [7] G. A. Dooley, A. H. G. Peter, M. Vogelsberger, J. Zavala, and A. Frebel, Mon. Not. R. Astron. Soc. 461, 710 (2016).
- [8] J. I. Read, M. G. Walker, and P. Steger, Mon. Not. R. Astron. Soc. 481, 860 (2018).
- [9] V. H. Robles, T. Kelley, J. S. Bullock, and M. Kaplinghat, Mon. Not. R. Astron. Soc. 490, 2117 (2019).
- [10] J. Zavala, M. R. Lovell, M. Vogelsberger, and J. D. Burger, Phys. Rev. D 100, 063007 (2019).
- [11] M. Kaplinghat, M. Valli, and H.-B. Yu, Mon. Not. R. Astron. Soc. 490, 231 (2019).
- [12] F. Kahlhoefer, M. Kaplinghat, T. R. Slatyer, and C.-L. Wu, J. Cosmol. Astropart. Phys. 12 (2019) 010.
- [13] E. O. Nadler, A. Banerjee, S. Adhikari, Y.-Y. Mao, and R. H. Wechsler, Astrophys. J. 896, 112 (2020).
- [14] H. C. Turner, M. R. Lovell, J. Zavala, and M. Vogelsberger, Mon. Not. R. Astron. Soc. 505, 5327 (2021).
- [15] C. A. Correa, Mon. Not. R. Astron. Soc. **503**, 920 (2021).
- [16] O. Sameie, M. Boylan-Kolchin, R. Sanderson, D. Vargya, P. Hopkins, A. Wetzel, J. Bullock, A. Graus, and V. Robles, Mon. Not. R. Astron. Soc. 507, 720 (2021).
- [17] O. Sameie, S. Chakrabarti, H.-B. Yu, M. Boylan-Kolchin, M. Vogelsberger, J. Zavala, and L. Hernquist, arXiv:2006 .06681.
- [18] P. Salucci, Astron. Astrophys. Rev. 27, 2 (2019).
- [19] A. V. Kravtsov, O. Y. Gnedin, and A. A. Klypin, Astrophys. J. 609, 482 (2004).
- [20] E. D'Onghia, V. Springel, L. Hernquist, and D. Keres, Astrophys. J. 709, 1138 (2010).
- [21] J. Peñarrubia, A. J. Benson, M. G. Walker, G. Gilmore, A. W. McConnachie, and L. Mayer, Mon. Not. R. Astron. Soc. 406, 1290 (2010).
- [22] G. A. Dooley, A. H. G. Peter, T. Yang, B. Willman, B. F. Griffen, and A. Frebel, Mon. Not. R. Astron. Soc. 471, 4894 (2017).
- [23] S. Garrison-Kimmel, A. Wetzel, J. S. Bullock, P. F. Hopkins, M. Boylan-Kolchin, C.-A. Faucher-Giguère,

- D. Kereš, E. Quataert, R. E. Sanderson, A. S. Graus *et al.*, Mon. Not. R. Astron. Soc. **471**, 1709 (2017).
- [24] J. Samuel, A. Wetzel, E. Tollerud, S. Garrison-Kimmel, S. Loebman, K. El-Badry, P. F. Hopkins, M. Boylan-Kolchin, C.-A. Faucher-Giguère, J. S. Bullock *et al.*, Mon. Not. R. Astron. Soc. 491, 1471 (2020).
- [25] S. Tulin and H.-B. Yu, Phys. Rep. 730, 1 (2018).
- [26] A. Kamada, M. Kaplinghat, A. B. Pace, and H.-B. Yu, Phys. Rev. Lett. 119, 111102 (2017).
- [27] P. Creasey, O. Sameie, L. V. Sales, H.-B. Yu, M. Vogelsberger, and J. Zavala, Mon. Not. R. Astron. Soc. 468, 2283 (2017).
- [28] T. Ren, A. Kwa, M. Kaplinghat, and H.-B. Yu, Phys. Rev. X 9, 031020 (2019).
- [29] M. Kaplinghat, T. Ren, and H.-B. Yu, J. Cosmol. Astropart. Phys. 06 (2020) 027.
- [30] J. Kummer, F. Kahlhoefer, and K. Schmidt-Hoberg, Mon. Not. R. Astron. Soc. 474, 388 (2018).
- [31] O. Sameie, H.-B. Yu, L. V. Sales, M. Vogelsberger, and J. Zavala, Phys. Rev. Lett. 124, 141102 (2020).
- [32] S. Balberg, S. L. Shapiro, and S. Inagaki, Astrophys. J. 568, 475 (2002).
- [33] J. Koda and P. R. Shapiro, Mon. Not. R. Astron. Soc. 415, 1125 (2011).
- [34] O. D. Elbert, J. S. Bullock, S. Garrison-Kimmel, M. Rocha, J. Oñorbe, and A. H. G. Peter, Mon. Not. R. Astron. Soc. 453, 29 (2015).
- [35] R. Essig, S. D. Mcdermott, H.-B. Yu, and Y.-M. Zhong, Phys. Rev. Lett. 123, 121102 (2019).
- [36] H. Nishikawa, K. K. Boddy, and M. Kaplinghat, Phys. Rev. D 101, 063009 (2020).
- [37] S. Y. Kim and A. H. G. Peter, arXiv:2106.09050.
- [38] J. L. Feng, M. Kaplinghat, H. Tu, and H.-B. Yu, J. Cosmol. Astropart. Phys. 07 (2009) 004.
- [39] A. Loeb and N. Weiner, Phys. Rev. Lett. 106, 171302 (2011).
- [40] M. Kaplinghat, S. Tulin, and H.-B. Yu, Phys. Rev. Lett. **116**, 041302 (2016).
- [41] S. Girmohanta and R. Shrock, Phys. Rev. D 106, 063013 (2022).
- [42] D. N. Spergel and P. J. Steinhardt, Phys. Rev. Lett. 84, 3760 (2000).
- [43] J. F. Navarro, C. S. Frenk, and S. D. M. White, Astrophys. J. 490, 493 (1997).
- [44] M. Kaplinghat, R. E. Keeley, T. Linden, and H.-B. Yu, Phys. Rev. Lett. 113, 021302 (2014).
- [45] O. Sameie, P. Creasey, H.-B. Yu, L. V. Sales, M. Vogelsberger, and J. Zavala, Mon. Not. R. Astron. Soc. 479, 359 (2018).

- [46] T. Kelley, J. S. Bullock, S. Garrison-Kimmel, M. Boylan-Kolchin, M. S. Pawlowski, and A. S. Graus, Mon. Not. R. Astron. Soc. 487, 4409 (2019).
- [47] S. B. Green, F. C. van den Bosch, and F. Jiang, Mon. Not. R. Astron. Soc. 503, 4075 (2021).
- [48] S. von Hoerner, Astrophys. J. 125, 451 (1957).
- [49] I. King, Astron. J. 67, 471 (1962).
- [50] S. B. Green, F. C. van den Bosch, and F. Jiang, Mon. Not. R. Astron. Soc. 503, 4075 (2021).
- [51] F. Jiang, A. Dekel, J. Freundlich, F. C. van den Bosch, S. B. Green, P. F. Hopkins, A. Benson, and X. Du, Mon. Not. R. Astron. Soc. 502, 621 (2021).
- [52] S. Chandrasekhar, Astrophys. J. 97, 255 (1943).
- [53] A. A. Dutton and A. V. Macciò, Mon. Not. R. Astron. Soc. 441, 3359 (2014).
- [54] M. Rocha, A. H. G. Peter, J. S. Bullock, M. Kaplinghat, S. Garrison-Kimmel, J. Oñorbe, and L. A. Moustakas, Mon. Not. R. Astron. Soc. 430, 81 (2013).
- [55] L. Sagunski, S. Gad-Nasr, B. Colquhoun, A. Robertson, and S. Tulin, J. Cosmol. Astropart. Phys. 01 (2021) 024.
- [56] G. D. Martinez, Q. E. Minor, J. Bullock, M. Kaplinghat, J. D. Simon, and M. Geha, Astrophys. J. 738, 55 (2011).
- [57] M. G. Walker, M. Mateo, E. W. Olszewski, S. Koposov, V. Belokurov, P. Jethwa, D. L. Nidever, V. Bonnivard, J. I. Bailey III, E. F. Bell *et al.*, Astrophys. J. **819**, 53 (2016).
- [58] J. I. Read and D. Erkal, Mon. Not. R. Astron. Soc. 487, 5799 (2019).
- [59] R. J. J. Grand, F. Marinacci, R. Pakmor, C. M. Simpson, A. J. Kelly, F. A. Gómez, A. Jenkins, V. Springel, C. S. Frenk, and S. D. M. White, Mon. Not. R. Astron. Soc. 507, 4953 (2021).
- [60] E. Patel, N. Kallivayalil, N. Garavito-Camargo, G. Besla, D. R. Weisz, R. P. van der Marel, M. Boylan-Kolchin, M. S. Pawlowski, and F. A. Gómez, Astrophys. J. 893, 121 (2020).
- [61] J. Bland-Hawthorn and O. Gerhard, Annu. Rev. Astron. Astrophys. 54, 529 (2016).
- [62] D. Harvey, A. Robertson, R. Massey, and I. G. McCarthy, Mon. Not. R. Astron. Soc. 488, 1572 (2019).
- [63] K. E. Andrade, J. Fuson, S. Gad-Nasr, D. Kong, Q. Minor, M. G. Roberts, and M. Kaplinghat, Mon. Not. R. Astron. Soc. 510, 54 (2021).

- [64] M. Meneghetti et al., Science 369, 1347 (2020).
- [65] Q. E. Minor, S. Gad-Nasr, M. Kaplinghat, and S. Vegetti, Mon. Not. R. Astron. Soc. 507, 1662 (2021).
- [66] D. Yang and H.-B. Yu, Phys. Rev. D 104, 103031 (2021).
- [67] J. Peñarrubia, J. F. Navarro, and A. W. McConnachie, Astron. Nachr. 329, 934 (2008).
- [68] E. Hayashi, J. F. Navarro, J. E. Taylor, J. Stadel, and T. Quinn, Astrophys. J. 584, 541 (2003).
- [69] A. Helmi, Annu. Rev. Astron. Astrophys. 58, 205 (2020).
- [70] A. F. Neto, L. Gao, P. Bett, S. Cole, J. F. Navarro, C. S. Frenk, S. D. M. White, V. Springel, and A. Jenkins, Mon. Not. R. Astron. Soc. 381, 1450 (2007).
- [71] B. Diemer and M. Joyce, Astrophys. J. **871**, 168 (2019).
- [72] Z.-Z. Li, Y.-Z. Qian, J. Han, T. S. Li, W. Wang, and Y. P. Jing, Astrophys. J. 894, 10 (2020).
- [73] S. Tulin, H.-B. Yu, and K. M. Zurek, Phys. Rev. D 87, 115007 (2013).
- [74] A. Robertson, R. Massey, and V. Eke, Mon. Not. R. Astron. Soc. 467, 4719 (2017).
- [75] A. Robertson, D. Harvey, R. Massey, V. Eke, I.G. McCarthy, M. Jauzac, B. Li, and J. Schaye, Mon. Not. R. Astron. Soc. 488, 3646 (2019).
- [76] J. Gan, X. Kang, F. C. van den Bosch, and J. Hou, Mon. Not. R. Astron. Soc. 408, 2201 (2010).
- [77] S. P. Fillingham, M. C. Cooper, T. Kelley, M. K. Rodriguez Wimberly, M. Boylan-Kolchin, J. S. Bullock, S. Garrison-Kimmel, M. S. Pawlowski, and C. Wheeler, arXiv:1906 .04180.
- [78] R. D'Souza and E. F. Bell, Mon. Not. R. Astron. Soc. 504, 5270 (2021).
- [79] A. D. Ludlow, S. Bose, R. E. Angulo, L. Wang, W. A. Hellwing, J. F. Navarro, S. Cole, and C. S. Frenk, Mon. Not. R. Astron. Soc. 460, 1214 (2016).
- [80] J. D. Simon, Astrophys. J. 863, 89 (2018).
- [81] J. E. Taylor and J. F. Navarro, Astrophys. J. 563, 483 (2001).
- [82] M. Rocha, A. H. G. Peter, J. S. Bullock, M. Kaplinghat, S. Garrison-Kimmel, J. Onorbe, and L. A. Moustakas, Mon. Not. R. Astron. Soc. **430**, 81 (2013).
- [83] Y. Ascasibar and S. Gottlöber, Mon. Not. R. Astron. Soc. **386**, 2022 (2008).
- [84] B. Colquhoun, S. Heeba, F. Kahlhoefer, L. Sagunski, and S. Tulin, Phys. Rev. D 103, 035006 (2021).